Icarus 416 (2024) 116086

Contents lists available at ScienceDirect

Icarus

journal homepage: www.elsevier.com/locate/icarus

Sublimation pressures of common volatiles at low temperature and maps of supervolatile cold traps on the Moon

Norbert Schörghofer [a,*], Jean-Pierre Williams [b]

[a] Planetary Science Institute, Honolulu, HI, USA
[b] Earth, Planetary, and Space Sciences, University of California, Los Angeles, CA, USA

ARTICLE INFO

Dataset link: https://doi.org/10.7910/DVN/UUIVXQ

Keywords:
Lunar surface
Physical properties (ice)
Surface ices
solid matter physics

ABSTRACT

Astrophysical processes can involve sublimation rates too low to be measured in the laboratory. Here, measured vapor pressures of solid H_2O, Ar, CO_2, H_2S, NH_3, SO_2, CH_4, HCN, CH_3OH, and C_2H_4 are reviewed, fitted, and robustly extrapolated to lower temperatures. Knowledge gaps regarding vapor pressures are identified for several chemical species. Maps of lunar cold traps for supervolatiles are presented based on sublimation rates time-averaged over diurnal and seasonal cycles of measured surface temperatures for the north and south polar region. The cold trap areas for these supervolatiles are all much smaller than for H_2O.

1. Introduction

Solar system processes can involve slow sublimation or deposition of ices, for example, the sublimation of volatiles from cold traps near the poles of the Moon and Mercury, condensation in protoplanetary disks, or activation of comets. On the Moon, sublimation could have taken place over the last few billion years (Arnold, 1979), and sublimation rates of less than 1 nm/yr are of interest as this allows for the retention and survival of volatiles on geologic timescales. Such low rates are challenging to measure in the laboratory, and have to be extrapolated from measurements at higher temperature. The latent heat of sublimation of a solid changes only slowly with temperature, which is the basis for robust extrapolations.

Here, the vapor pressures of ten volatiles are reviewed, fitted, and extrapolated to lower temperatures. Species selected are those detected by the LCROSS mission (Colaprete et al., 2010): H_2O, H_2S, NH_3, SO_2, C_2H_4, CO_2, CH_3OH, and CH_4 (in order of observed abundance). These species are also found in comets (Bockelée-Morvan and Biver, 2017). We also include argon, which has long been observed in the lunar exosphere (Stern, 1999) and can be produced by radioactive decay of potassium or implanted by solar wind.

A subset of these results is then applied to produce maps of lunar cold traps for supervolatiles. Species more volatile than H_2O are known as supervolatiles or hypervolatiles. Two improvements in methodology, updated sublimation pressure parametrizations and use of time-averaged sublimation rates, result in more accurate maps of supervolatiles than produced previously (Landis et al., 2022). The results reveal widespread cold-trapping for a few chemical species, while others are not expected to be cold-trapped on the Moon. The maps can also be utilized for landing site selections.

2. Sublimation pressures: data sources and equations

2.1. Literature (data sources)

Various reference works are available that contain abundant information about vapor pressures of solids and low-temperature phases. The International Critical Tables (Washburn et al., 1933) are a comprehensive reference for material properties, but have not been updated since 1933. Stull (1947b,a) compiled vapor pressure data for 1200 organic and 300 inorganic compounds, and tabulated the fitted data sets. Fray and Schmitt (2009) reviewed vapor pressure data for 53 astrophysically relevant species and found vapor pressure data for the solid phase for 30 of them. Unfortunately they fitted the data with polynomials in powers of $1/T$, and hence the fits cannot be used for extrapolations to lower temperatures. The NIST Chemistry Webbook (Linstrom and Mallard, 2001) maintains an extensive online database, including phase change data. The National Institute of Standards and Technology (NIST) also provides https://trc.nist.gov/thermolit/, a database of relevant literature sources (Kazakov et al., 2012).

In a series of reports, Ziegler et al. (1962a,b,c) and Mullins et al. (1963) reviewed existing measurements and calculated interpolated

* Corresponding author.
E-mail address: norbert@psi.edu (N. Schörghofer).

https://doi.org/10.1016/j.icarus.2024.116086
Received 22 February 2024; Received in revised form 9 April 2024; Accepted 10 April 2024
Available online 16 April 2024

and extrapolated vapor pressures, taking the temperature-dependent latent heat and heat capacity into account, which were also parametrized. Their extrapolations are hence more reliable than those based purely on fits to measured vapor pressures.

Huebner et al. (2006) provides vapor pressure coefficients for various volatiles relevant to comets. Yu et al. (2023) have recently compiled vapor pressure data of organic solids relevant to Titan. The present work is motivated by applications to the Moon, and the robustness of extrapolation formulae is a prime concern.

2.2. Vapor pressure equations

The sublimation rate into vacuum is closely related to the vapor pressure of the solid, as will be described in Section 2.3. To extrapolate the vapor pressure p beyond the temperature range it has been measured, a robust physics-based parametrization is desirable. The Clausius–Clapeyron relation is

$$\frac{d\ln p}{dT} = \frac{L_{\rm ice}}{k_B T^2} \quad \text{or} \quad \frac{d\ln p}{d(1/T)} = -\frac{L_{\rm ice}}{k_B} \tag{1}$$

where $L_{\rm ice}$ is the latent heat of sublimation and k_B the Boltzmann constant. The molar volume of the solid relative to that of the vapor is neglected. When $L_{\rm ice}$ is temperature-independent, the Clausius–Clapeyron equation results in

$$\ln p = A - \frac{L_{\rm ice}}{k_B T} \qquad \text{(August Equation)} \tag{2}$$

A temperature dependence of the latent heat can be introduced in the form

$$\frac{L_{\rm ice}}{k_B} = b_1 + b_2 T + b_3 T^2 + \cdots \tag{3}$$

where b_1 corresponds to the latent heat at absolute zero. Integration of the Clausius–Clapeyron equation then leads to

$$\ln p = b_0 - \frac{b_1}{T} + b_2 \ln T + b_3 T + \cdots \tag{4}$$

This generates terms proportional to $1/T$ and $\log(T)$, in addition to a polynomial in T. With the first three terms, the equation is sometimes known as Rankine–Dupre formula. With four terms, it is known as the Nernst Equation.

A widely used empirical approximation with three parameters is

$$\ln p = A - \frac{B}{T+C} \qquad \text{(Antoine Equation)} \tag{5}$$

but it does not have the desired limit for $T \to 0$, which should be $p \to 0$ for any solid. A few investigators (Brown and Ziegler, 1980; Fray and Schmitt, 2009) use expansions in negative powers of T,

$$\ln p = a_0 - \frac{a_1}{T} + \frac{a_2}{T^2} + \frac{a_3}{T^3} + \cdots \tag{6}$$

which are even more ill-behaved for low temperature extrapolations.

At low temperature, the vapor pressure and sublimation pressure become very small and therefore difficult to measure. A more robust approach is extrapolation based on the latent heat of sublimation, especially when combined with measurements of the heat capacity. Appendix A.1 describes further theoretical justification for Eq. (4).

2.3. Sublimation rate

The sublimation rate into vacuum is calculated from the vapor pressure with the Hertz–Knudsen equation (Persad and Ward, 2016), sometimes also called the Hertz–Knudsen–Langmuir equation:

$$E = \alpha(T)\, p(T) \sqrt{\frac{m}{2\pi k_B T}} \tag{7}$$

Here, m is the mass of a molecule and α is the sublimation coefficient. The coefficient α depends on the fraction of elastic collisions and the surface roughness, and it is by itself temperature dependent. At low temperature though it tends toward 1 (e.g., Levenson, 1971; Haynes et al., 1992).

The Hertz–Knudsen equation arises from the flux in an ideal gas $(1/4)n\bar{v}$, with the mean velocity

$$\bar{v} = \sqrt{8k_B T/\pi m} \tag{8}$$

Combined with the ideal gas law, and after multiplication with αm, this results in Eq. (7). The velocity distribution of molecules emitted from the surface is to leading order the same as in a collisional ideal gas, following the Knudsen Cosine Law, (e.g., Knudsen, 1909; Comsa, 1968; Feres and Yablonsky, 2004). Hence, expression (7) is still valid even if no collisions take place in the gas.

Vapor pressure measurements are more common than measurements of the sublimation rate into vacuum. Comparison of the two provides a measurement of α.

The primary motivation for this work are lunar cold traps. For cold trapping, relevant sublimation rates are as low as 1 mm/Ga. For water ice, this value corresponds to about 1 kg m^{-2} Ga^{-1}. For the ranges of molecular masses and threshold temperatures considered in this work, this rate corresponds to a vapor pressure of roughly 10^{-14} Pa, which is below the range of vapor pressures typically measured in laboratories.

2.4. Fitting procedure

In this work, Eq. (4) is fitted to the data, using the first two or three terms, depending on the temperature range of the available data. The fit is a least-square fit to the logarithm of the pressures, which emphasizes relative errors. It also makes it a linear rather than a non-linear regression.

Since the fits are based on linear regression, an error bar can be readily produced for each coefficient. These errors are highly correlated and cannot be used to estimate the uncertainties of the vapor pressure. However, they are used to determine the number of significant digits. The leading uncertainties for extrapolations to low temperature, are either the lack of data or contradictory measurements.

For each fit, the data are shown with $1/T$ on the horizontal axis and a base-10 logarithm on the vertical axis. Although the horizontal axis scale is $1/T$, for clarity, the axis ticks are labeled with the T values. A separate plot shows the ratio of the data relative to the fit. To achieve a balanced weighing among data sets, some data are downsampled for the fits. Some authors (e.g., Stull, 1947a,b; Tickner and Lossing, 1951) provide data equally spaced in vapor pressure, based on a fit to their compiled measurements.

In total ten chemical species are considered. For H_2O and CH_3OH, the vapor pressures have been recently reviewed and robustly fitted, while for the other eight species new fits to multiple data sets are presented.

3. Vapor pressures for individual species

3.1. H_2O (water)

Murphy and Koop (2005) reviewed the vapor pressure of ice and recommend the following parametrizations above 110 K:

$$b_0 = 28.9074,\ b_1 = 6143.7 \qquad \text{(2-parameter)} \tag{9}$$

$$b_0 = 9.550426,\ b_1 = 5723.265,\ b_2 = 3.53068,\ b_3 = -0.00728332 \qquad \text{(4-parameter)} \tag{10}$$

This parametrization also closely matches the more recent measurements by Bielska et al. (2013).

In 1954, the Kelvin temperature scale was defined by the triple point of water as exactly 273.16 K, a testament to how accurately the triple point can be measured. This fixed point was abandoned with the International Temperature Scale of 1990 (ITS-90). The ITS-90 formulation of the vapor pressure down to −150 °C is given in Hardy

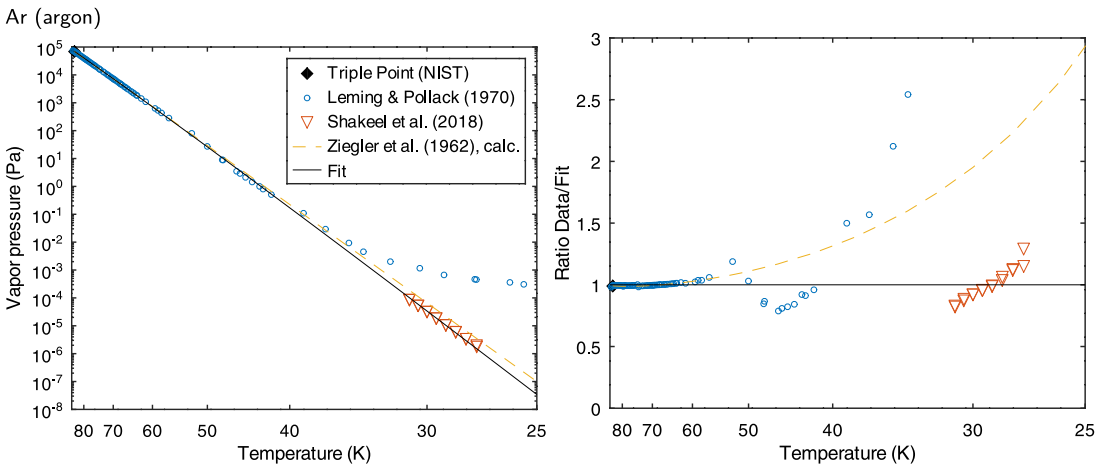

Fig. 1. Vapor pressure of solid argon (Ar). Data used for fitting are the triple point, the data from Leming and Pollack (1970) restricted to temperatures above 50 K (although the remaining data points are still included in the plot of residuals), and the data by Shakeel et al. (2018). The 3-parameter fit (11) is also shown.

(1998), using coefficients b_0 to b_5. The parametrization by Murphy and Koop (2005) is preferred here, because it is more recent and extends to slightly lower temperatures.

Amorphous ice can start to form below about 140 K (Sack and Baragiola, 1993). The transition temperature depends on the rate of deposition and is lower for slower deposition (Jenniskens et al., 1998). Amorphous ice can have various forms and sublimation rates, resulting in an intrinsic uncertainty about the pertinent sublimation rate. Ice could have been deposited at a different temperature from its current environment, and could be crystalline or amorphous in nature. If the ice is in its standard hexagonal crystal form, the coefficients above (9), (10) can be used for extrapolation to low temperature. Leger et al. (1983) provided a theoretical expression for the vapor pressure of amorphous ice and found it to be only moderately higher. For example, the vapor pressure of crystalline ice at 100 K is the same as for amorphous ice at 97 K. Sack and Baragiola (1993) measured slightly enhanced sublimation rates for partially amorphized ice films.

The higher vapor pressures by Bryson et al. (1974) are thought to be due to amorphization (Murphy and Koop, 2005). Mauersberger and Krankowsky (2003) argued that below 169 K the vapor pressure of ice deviates from the trend at higher temperatures, but this claim conflicts with multiple other data sets. The recent measurements by Shakeel et al. (2018) in the range of 155–161 K are 38%–78% above the results from Murphy and Koop (2005). Overall, the main uncertainty in extrapolating sublimation rates to low temperature is potential phase changes. Five low pressure phases are known for ice: I_h, I_c, I_ar, I_al, and I_ah (Jenniskens et al., 1998).

3.2. Ar (argon)

Tegeler et al. (1999) review ten data sets for the sublimation pressure of solid argon. Among those, only the measurements by Leming and Pollack (1970) reach below 66 K. Recently, Shakeel et al. (2018) measured sublimation pressures in the range of 20.5–28.2 K. Fig. 1 shows these data.

Here, the data from Leming and Pollack (1970) were restricted to temperatures above 50 K for the fit. The latent heat of argon is thought to vary little with temperature (Beaumont et al., 1961). The 3-parameter fit is

$$b_0 = 30.9 \pm 0.9, b_1 = 1076 \pm 9, b_2 = -1.6 \pm 0.2 \quad (11)$$

The slope of the data by Shakeel et al. (2018) is inconsistent with the slope at higher temperature (Fig. 1, residuals), and this may constitute the leading uncertainty. The integrations by Ziegler et al. (1962b) also result in higher vapor pressures than measured by Shakeel et al. (2018).

3.3. CO_2 (carbon dioxide)

The experimental data used for this fit (Fig. 2) are from Stull (1947a), Tickner and Lossing (1951), Bryson et al. (1974) and Fernández-Fassnacht and Del Río (1984) and Shakeel et al. (2018). The comprehensive review by Stull (1947a) already takes into account earlier measurements. Fitting of the data results in the following coefficients:

$$b_0 = 32.6 \pm 1.4, b_1 = 3292 \pm 31, b_2 = -0.08 \pm 0.02 \quad (12)$$

The integrations by Mullins et al. (1963) match the data by Bryson et al. (1974), although they predate these measurements (Fig. 2, residuals). The discrepancy between the low-temperature data by Bryson et al. (1974) and Shakeel et al. (2018) is a source of uncertainty for extrapolation to even lower temperatures.

Solid CO_2 remains in its cubic form down to at least 50 K, where a glass transition occurs (Falk, 1987; Souda, 2006). Amorphous CO_2 ice converts to the crystalline form at 30 K (Escribano et al., 2013). No measurements of the vapor pressure of amorphous CO_2 were found.

3.4. H_2S (hydrogen sulfide)

Solid H_2S has three phases at low pressure (Shimizu et al., 1991, 1995). The lowest temperature phase (III), which exists below 103.5 K, is tetragonal, whereas phase II (103.5–126.2 K) and phase I (from 126.2 K to the triple point at 187.6 K) are both cubic.

Data from Giauque and Blue (1936) and Clark et al. (1951) are shown in Fig. 3. The fit for phase I is

$$b_0 = 24.45 \pm 0.05, b_1 = 2702 \pm 7 \quad (13)$$

For comparison, Clark et al. (1951) when converted into Pascal and exponential base provide $b_0 = 24.47$, $b_1 = 2706$. Clark et al. (1951) also provides a fit for phase II, which is not repeated here. Sublimation pressure measurements for phase III appear to be missing from the literature entirely.

The vapor pressure changes continuously across phase transitions, so from the phase II data in Fig. 3, it is apparent that the vapor pressure of phase III is likely far higher than the extrapolated vapor pressure from phase I.

3.5. NH_3 (ammonia)

Stull (1947a) has compiled laboratory measurements for the vapor pressure of solid and liquid ammonia, with at least 9 sources for the solid phase. Also plotted in Fig. 4 are data that include measurements

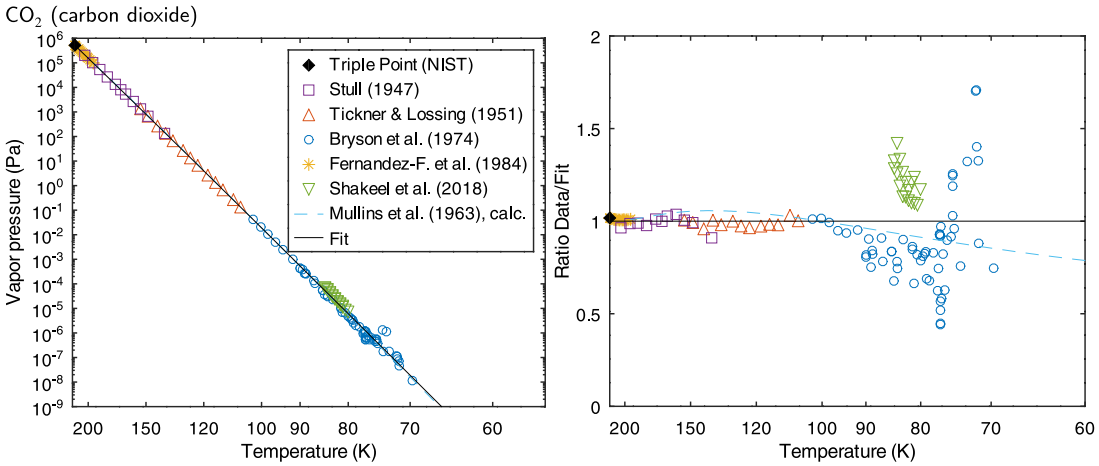

Fig. 2. Vapor pressure of solid carbon dioxide (CO_2). The fit is based on the data by Stull (1947a) and Tickner and Lossing (1951), the triple point from NIST, and downsampled values from Bryson et al. (1974), Fernández-Fassnacht and Del Río (1984) and Shakeel et al. (2018). The low-temperature measurements by Bryson et al. (1974) have considerable spread and deviate from those of Shakeel et al. (2018). For these two sources, the published fits to the data are evaluated at four temperatures each (not shown, but used during fitting).

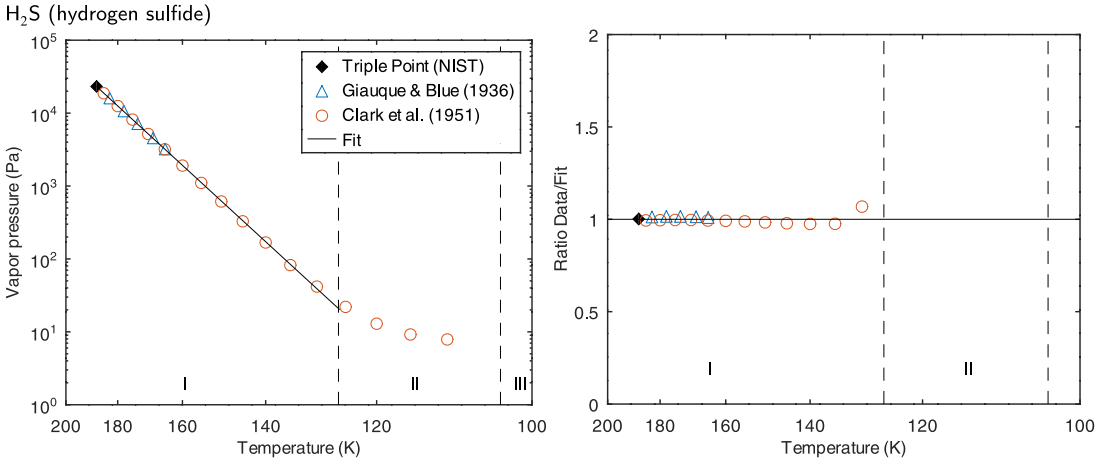

Fig. 3. Vapor pressure of solid hydrogen sulfide (H_2S). Vertical dashed lines indicate phase transition temperatures.

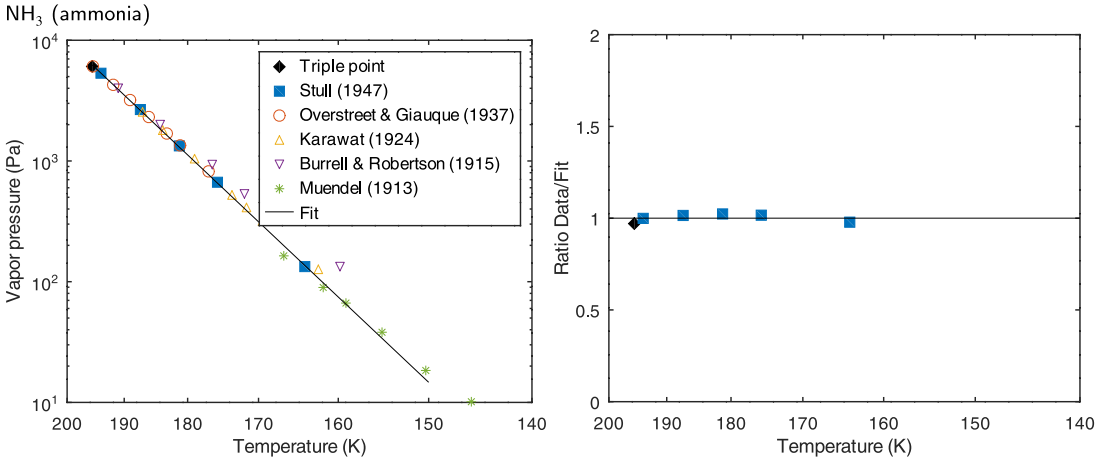

Fig. 4. Vapor pressure of solid ammonia (NH_3). Only the data by Stull (1947a) are used for the fit, as the earlier data sets were already incorporated in their tabulated data. Only the data used for the fit are included in the plot of ratios. Triple point from Staveley et al. (1981).

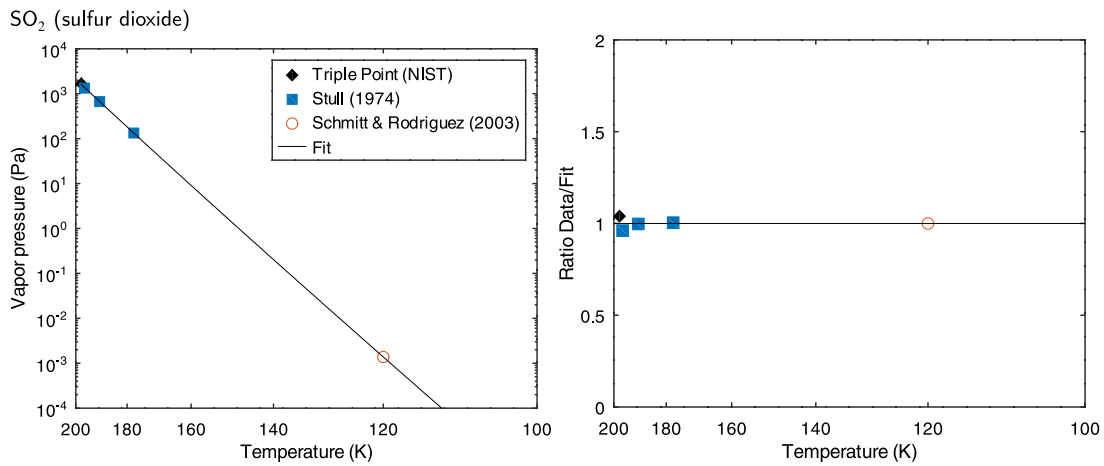

Fig. 5. Vapor pressure of solid sulfur dioxide (SO_2). The triple point from NIST traces back to Giauque and Stephenson (1938). The three-parameter fit is shown.

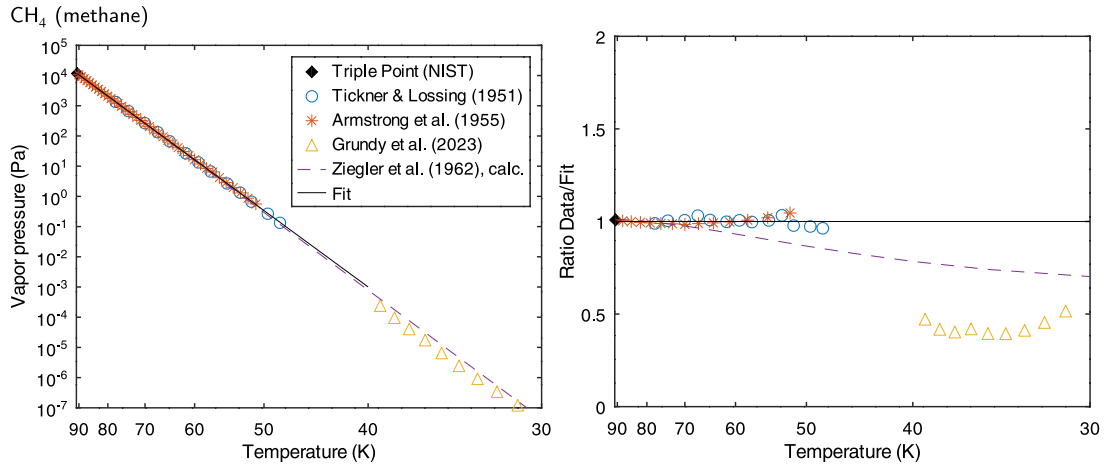

Fig. 6. Vapor pressure of solid methane (CH_4). The data by Grundy et al. (2023) are omitted from the fit, but nevertheless included in the residual plot. The fit is based on the triple point, the data by Tickner and Lossing (1951), and one third of the data points by Armstrong et al. (1955) to create a data set with a proportional number of data points.

below −100 °C (Karwat, 1924; Burrell and Robertson, 1915; Mündel, 1913), although the fit by Stull is based on additional measurements. The two-parameter fit is

$$b_0 = 28.7 \pm 0.2, b_1 = 3903 \pm 30 \quad (14)$$

The cubic crystalline phase of ammonia has been observed to transition into an amorphous phase at 57 K (Zheng and Kaiser, 2007).

3.6. SO_2 (sulfur dioxide)

Vapor pressure measurements for solid SO_2 are rare. Stull (1947a) reviews the preceding published data. Schmitt and Rodriguez (2003) added one sublimation rate measurement, which was then converted to a vapor pressure. Fig. 5 shows the data. The 3-parameter fit is

$$b_0 = 9 \pm 14, b_1 = 3775 \pm 361, b_2 = 3 \pm 2 \quad (15)$$

The result critically relies on the one data point by Schmitt and Rodriguez (2003).

3.7. CH_4 (methane)

Data for solid methane from Tickner and Lossing (1951), Armstrong et al. (1955) and Grundy et al. (2023) are shown in Fig. 6. The low-temperature measurements by Grundy et al. (2023) are systematically offset from the trend in the other data sets, and could not be consistently included even with a 3-parameter fit. Hence, they are omitted from the fit. The two-parameter fit is:

$$b_0 = 22.22 \pm 0.02, b_1 = 1164 \pm 1 \quad (16)$$

Extrapolations by Ziegler et al. (1962c) are also available for methane and trend in the same direction as those by Grundy et al. (2023), but to a smaller degree.

Methane undergoes a phase transition at 20.5 K to another cubic crystalline phase (Vogt and Pitzer, 1976), so the parametrization is only valid down to this temperature.

3.8. HCN (hydrogen cyanide)

Vapor pressures for solid HCN are available from Stull (1947a) and Appleton and Van Hook (1982). Noting the lack measurements at low temperatures, Hudson and Gerakines (2023) have obtained measurements at 121–139 K. Their fit, which combines the previous and their own measurements resulted in $\ln(p) = 26.50 - 4568/T$, when converted into Pascal. However, these data are significantly offset from a two-parameter fit to the data by Stull (1947a), and both combined cannot be fit well even with a 3-parameter fit.

Fig. 7 shows the data. Fitting only the data by Stull (1947a) yields

$$b_0 = 27.03 \pm 0.07, b_1 = 4472 \pm 17 \quad (17)$$

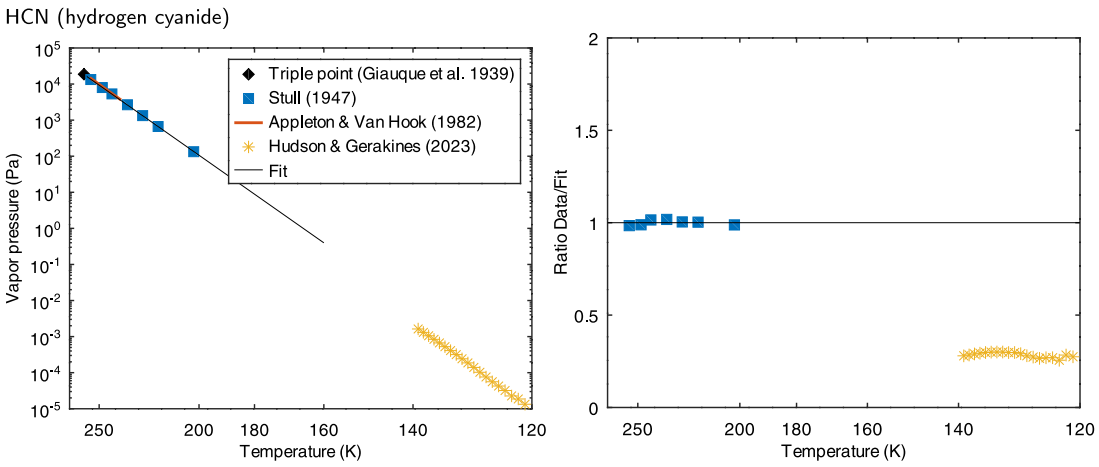

Fig. 7. Vapor pressure of solid hydrogen cyanide (HCN). Only the data by Stull (1947a) are used for the fit, but the data by Hudson and Gerakines (2023) are included in the plot of residuals. Triple point from Giauque and Ruehrwein (1939).

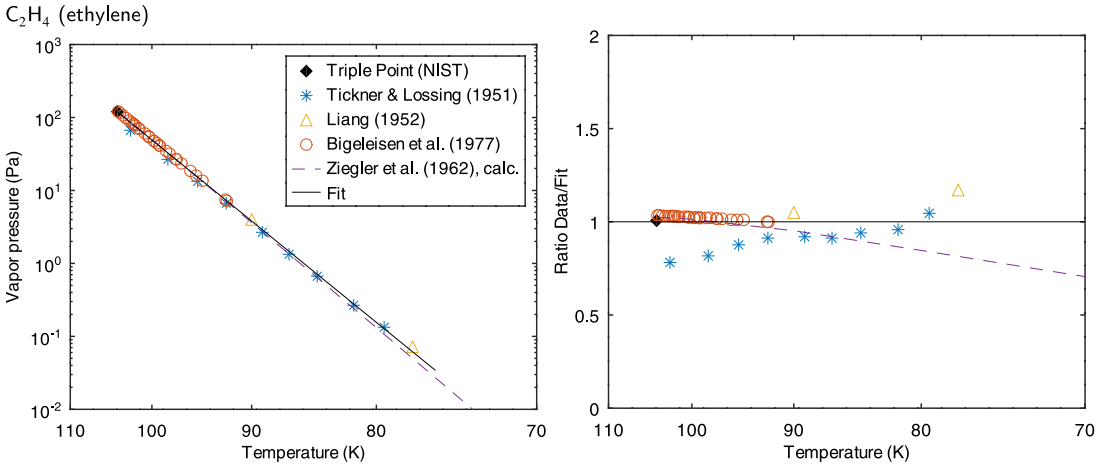

Fig. 8. Vapor pressure of solid ethylene (C_2H_4). The integrations by Ziegler et al. (1962a) are more consistent with the measurements by Bigeleisen et al. (1977) than with the other two data sets, but all three data sets and the triple point are used for the fit.

3.9. CH_3OH (methanol)

Methanol has two solid phases, the α-phase below 157.4 K and the β-phase from 157.4 K to the triple point at 175.6 K. Curiously, not even (Stull, 1947b) lists any measurements for methanol. Lucas et al. (2005) measured the sublimation pressures and arrive at the following parametrizations (converted to Pascal),

$$b_0 = 15.94, b_1 = 2453 \qquad \alpha\text{-phase} \tag{18}$$

$$b_0 = 15.02, b_1 = 2308 \qquad \beta\text{-phase} \tag{19}$$

3.10. C_2H_4 (ethylene)

Data used for fitting are from Tickner and Lossing (1951), Liang (1952) and Bigeleisen et al. (1977) along with the triple point. Fig. 8 shows the data and the fit. The residuals indicate inconsistent trends among the data sets, but the overall uncertainty is not large. The fitted coefficients are

$$b_0 = 26.9 \pm 0.1, b_1 = 2302 \pm 13 \tag{20}$$

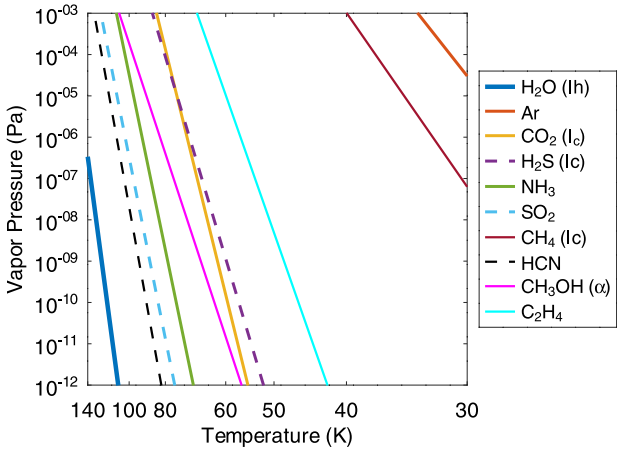

Fig. 9. Vapor pressures, some of them extrapolated. Dashed lines are for species that are particularly uncertain.

4. Synthesis of sublimation pressures

Vapor pressure graphs for all ten chemical species reviewed in Section 3 are combined in Fig. 9. Water has the lowest vapor pressure, and is therefore expected to be relatively abundant, as has long be realized by Watson et al. (1961). Sulfur dioxide and hydrogen cyanide are the next least volatile species, but the extrapolated vapor pressures are uncertain for both. Hydrogen sulfide is slightly more volatile than

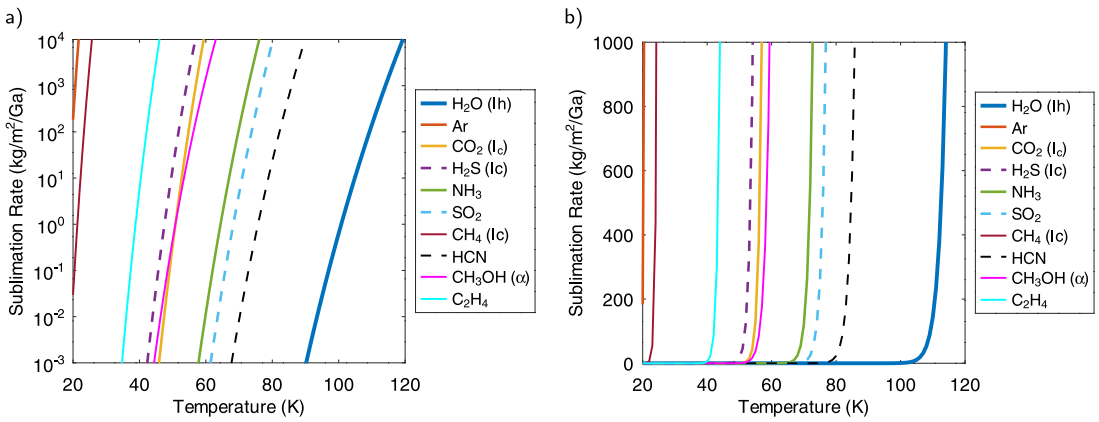

Fig. 10. Sublimation rates on logarithmic (a) and linear (b) vertical axes. Dashed lines are for those that are particularly uncertain.

Table 1
Threshold temperatures for four sublimation thresholds, sorted by volatility. The results by Zhang and Paige (2010) are based on a threshold of 1 kg m^{-2} Ga^{-1}.

Species	Threshold (K)				
(phase)	1 kg m^{-2} Ga^{-1}	10 kg m^{-2} Ga^{-1}	100 kg m^{-2} Ga^{-1}	1000 kg m^{-2} Ga^{-1}	Zhang and Paige (2010)
H_2O (Ih)	101	105	109	114	106.6
HCN	76	79	82	86	80.5
SO_2	70	73	76	79	62.3
NH_3	64	67	70	73	65.5
CH_3OH	51	53	56	59	–
CO_2	51	53	55	57	54.3
H_2S (Ic)	48	50	52	54	50.6
C_2H_4	39	40	42	44	–
CH_4 (Ic)	21.3	22.3	23.3	24.4	22.0
Ar	18.1	18.9	19.8	20.7	19.5

CO_2 if it is in phase I, but at the relevant temperatures, the equilibrium phase of H_2S is III, which is probably more volatile. Argon and methane have the highest and second highest vapor pressures, respectively, among the species considered.

Sublimation rates are calculated with the Hertz–Knudsen equation, assuming a sublimation coefficient of 1. Where measured (H_2O, Ar, CO_2) (Levenson, 1971; Haynes et al., 1992), this coefficient is known to be close to 1 at low temperature. Fig. 10 shows the sublimation rates on a logarithmic and a linear vertical axis. Use of a linear axis illustrates the concept of a sublimation threshold for the temperature.

Table 1 shows these thresholds for various sublimation rates. A comparison is made with the widely-used temperature thresholds by Zhang and Paige (2009, 2010). The largest deviation to their results is for sulfur dioxide, due to the addition of a single measured data point by Schmitt and Rodriguez (2003), so the results for SO_2 have to be treated with caution. All the threshold temperatures listed are below the minimum temperature the vapor pressure has ever been measured for the respective species.

Knowledge gaps exist for several of the chemical species. Measurements of the vapor pressure of sulfur dioxide below −100 °C are lacking almost entirely. No measurements are available for phase III of hydrogen sulfide. And if recent measurements of the sublimation pressure of hydrogen cyanide by Grundy et al. (2023) are correct, HCN is less volatile than assumed here. Overall, the largest uncertainties identified are for SO_2, H_2S (III), and HCN. Some of these uncertainties might be addressable with quantum chemistry calculations (e.g., Červinka and Beran, 2019).

5. Lunar cold traps for supervolatiles

Volatiles may be cold trapped in permanently shadowed craters on the Moon and are potential resources for sustained presence on the Moon (Arnold, 1979). At low temperature the sublimation rate into vacuum becomes lower than plausible long-term supply rates of these volatiles and ice can accumulate. The relevant threshold for the sublimation rate is ultimately determined by the amount that was delivered to the cold traps over time. These amounts are uncertain (e.g., Berezhnoy et al., 2012; Mandt et al., 2022), but temperature is only a slowly growing function of the sublimation rate, and the cold trap area depends only weakly on the threshold.

Landis et al. (2022) produced maps of cold traps for various supervolatiles poleward of 60° latitude for both polar regions using peak Diviner temperatures. Using time-averaged sublimation rates instead, Schorghofer and Williams (2020) and Schorghofer et al. (2021) published maps of water ice and CO_2 cold traps in the south polar region of the Moon. Here, we produce maps of supervolatiles for the five least volatile supervolatiles in Table 1: HCN, SO_2, NH_3, CH_3OH, and CO_2.

5.1. Diviner temperature data processing

The Diviner Lunar Radiometer Experiment is an infrared and solar radiometer onboard NASA's Lunar Reconnaissance Orbiter (LRO) (Paige et al., 2010a). It has a spectral range of 0.35–400 μm in nine spectral channels. Variations in LRO's altitude above the south pole have remained relatively stable during the majority of the mission at ∼40 km, with a cross-track width of ∼140 m and an in-track length of ∼400 m (Williams et al., 2016). In the north polar region the altitude has been more varied near the apoapsis of LRO. After an initial commissioning phase, the altitude varied between ∼50 km and ∼70 km during a ∼2 year period when the spacecraft was maintained in a near-circular orbit. LRO was then transitioned to a low fuel consumption elliptical orbit, or frozen orbit, with an apoapsis ∼190 km. Over time, the apoapsis has migrated to lower altitudes and over the

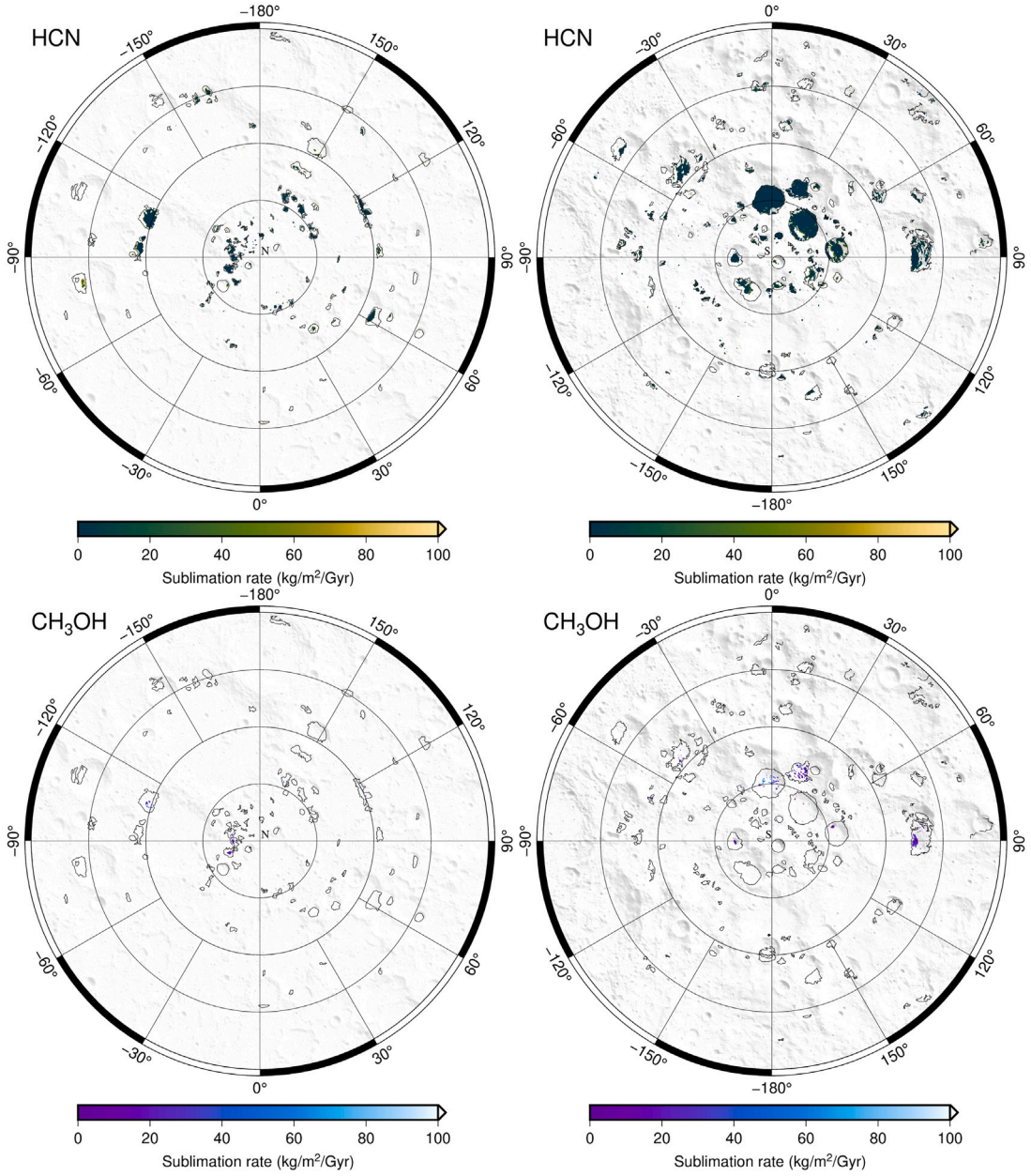

Fig. 11. Map of cold traps for carbon-bearing species hydrogen cyanide and methanol in the north and south polar regions of the Moon poleward of 80° latitude based on time-averaged sublimation rates. Black contours are for water ice cold traps determined from the same temperature data set. The grayscale background maps is topographic relief. (For interpretation of the references to color in this figure legend, the reader is referred to the web version of this article.)

last several years the periapsis altitude has increased resulting in a nearly circular orbit for LRO's current extended mission which began in Sept. 2022. This is providing the lowest altitude observations of the north polar region (~95 km) since the start of the frozen orbit (Petro et al., 2022).

The calibrated radiance measurements from Diviner channels 3–9 covering wavelengths from 7.55 to 400 μm were map projected onto a polar stereographic grid from 80° to 90° latitude and converted to bolometric brightness temperatures (Paige et al., 2010b). The pixel size at the pole is 240 m/pixel. During the draconic year (346.62 Earth days), the declination of the sun changes between ±1.5°, the equivalent of seasons. The Diviner Reduced Data Records (RDR) were compiled into 96 subsolar longitude bins and two subsolar latitude bins. For the south polar region, the Diviner data set used in this study was produced by Williams et al. (2019), spanning from July 2009 to February 2019. For the north polar region, new temperature maps were produced using data from July 2009 to January 2024 to include more recent, lower altitude observations from the current extended mission and the higher concentration of orbit ground tracks at lower-latitude polar regions ~85° resulting from the evolution of the spacecraft's declining orbital inclination (Petro et al., 2022). The inclusion of new data has improved the spatial coverage ~7% for all subsolar longitude bins.

To fill empty time bins due to incomplete time coverage, interpolation was used as described in Schorghofer and Williams (2020). We calculate time-average sublimation rates by averaging sublimation rates calculated for each of the 2 × 96 time bins for each pixel. In addition to the time-average, the maximum sublimation rate is also stored. A threshold for the maximum sublimation rate is equivalent to a threshold for the maximum temperature. Seasonal temperature amplitudes are particularly large in very cold areas (Schorghofer and

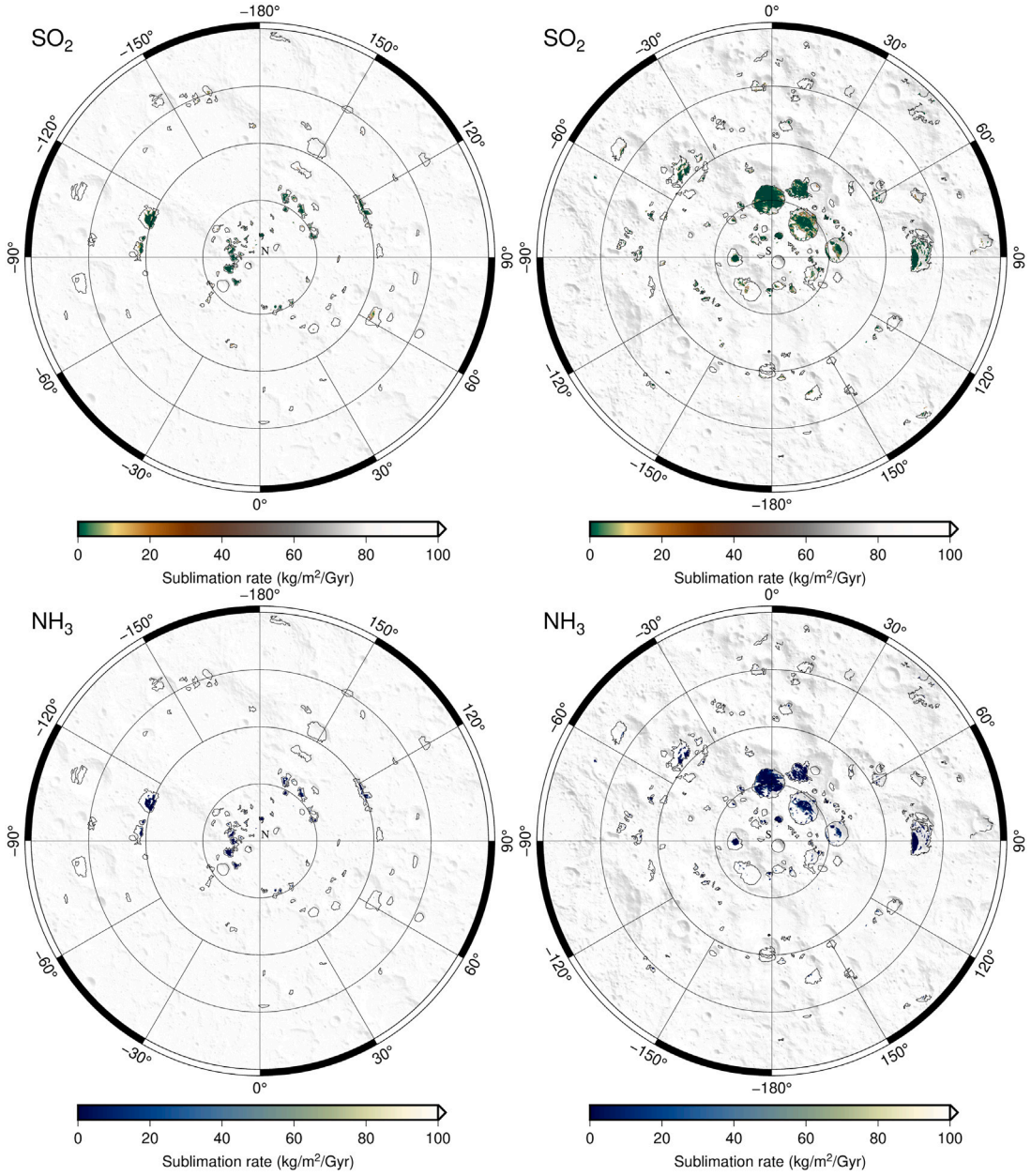

Fig. 12. Map of cold traps for sulfur dioxide and ammonia in the north and south polar regions of the Moon poleward of 80° latitude based on time-averaged sublimation rates. Black contours are for water ice cold traps determined from the same temperature data set. (For interpretation of the references to color in this figure legend, the reader is referred to the web version of this article.)

Williams, 2020), so it is crucial to include them for mapping the cold traps of supervolatiles.

Diviner has extensive spatial and temporal coverage, but specific solar azimuths could still be missed. For that reason, it is possible that cold traps are smaller than determined here.

5.2. Lunar maps for supervolatiles

Figs. 11 and 12 show maps of supervolatile cold traps for north and south polar regions of the Moon. Areas where sublimation rates are below 100 $\mathrm{kg\,m^{-2}\,Ga^{-1}}$ are colored. Maps for the carbon-bearing species HCN and CH_3OH are shown in Fig. 11. Based on the extensive size of its cold trap area, hydrogen cyanide may be the most widespread source of carbon on the Moon. The concentration of carbon in Apollo samples is very small (Gibson, 1977). CO_2, not shown, is slightly more volatile than CH_3OH, and its cold traps smaller. Methanol and carbon dioxide are expected to be cold-trapped only in small but contiguous regions, especially in the south polar region (see also Schorghofer et al., 2021; Landis et al., 2022).

Cold traps are widespread for SO_2 and NH_3 (Fig. 12). The large area for SO_2 is in part reliant on a change to the sublimation pressure data brought about by a single data point, and hence uncertain.

Table 2 lists total cold trap areas for various species and multiple sublimation thresholds. Significant cold traps areas exist for HCN, SO_2, and NH_3, although they are all much smaller than for H_2O. Only a minor fraction of the areas that are expected to have cold-trapped H_2O can also be expected to have cold-trapped supervolatiles. Moreover, the source abundance of H_2O may have been much larger than for other ices. For that reason, the majority of ice reservoirs can be expected to consist of only H_2O ice.

The cold trap area determined from time-averaged sublimation rates is necessarily larger compared to using the maximum sublimation rate,

Table 2
Cold traps areas for supervolatiles in the north and south polar region poleward of 80° latitude. The results by Landis et al. (2022) are based on maximum temperature and a threshold of 1 kg m^{-2} Ga^{-1} and here also limited to 80° latitude.

Threshold (kg m^{-2} Ga^{-1})	Area, north (km^2)					Area, south (km^2)				
	mean$_t(E)$			max$_t(E)$	Landis+	mean$_t(E)$			max$_t(E)$	Landis+
	1	10	100	1	(2022)	1	10	100	1	(2022)
H_2O (water)	5567	6519	7495	3931	5414	12 849	14 644	16 546	9864	11 434
HCN (hydrogen cyanide)	954	1264	1760	579	894	4 103	5 078	6 128	2598	3 305
SO_2 (sulfur dioxide)	585	761	1013	329	38	2 546	3 322	4 288	1319	273
NH_3 (ammonia)	336	462	599	135	99	1 326	1 927	2 616	571	554
CH_3OH (methanol)	11	29	84	1	–	52	136	358	8	–
CO_2 (carbon dioxide)	7	15	31	1	0	36	70	148	8	20

as the maximum is only reached for a short time each Draconic year. A column is added in Table 2 to illustrate these differences. For this reason, our cold traps for supervolatiles are larger than determined by Landis et al. (2022), but comparable when using the maximum as threshold instead. The large difference for SO_2 is due to the updated (and still uncertain) parametrization in sublimation pressures.

Argon and methane (that have both been detected in the lunar exosphere) cannot accumulate from year to year in ice form. These species can reside on the surface only in adsorbed form.

CRediT authorship contribution statement

Norbert Schörghofer: Writing – review & editing, Writing – original draft, Visualization, Methodology, Investigation, Funding acquisition, Formal analysis, Conceptualization. **Jean-Pierre Williams:** Writing – review & editing, Investigation, Funding acquisition, Formal analysis, Data curation.

Declaration of competing interest

The authors declare that they have no known competing financial interests or personal relationships that could have appeared to influence the work reported in this paper.

Data availability

The maps are available in digital form at https://doi.org/10.7910/DVN/UUIVXQ (Schorghofer and Williams, 2024).

Acknowledgments

This material is based upon work supported by the National Aeronautics and Space Administration, USA under grant No. 80NSSC22K1339 issued through the Lunar Data Analysis Program.

Appendix

A.1. Vapor pressure theory

A general theoretical form for the temperature dependence of the vapor pressure is Salter (1963), Reif (1965) and Leger et al. (1983)

$$p = \left(\frac{2\pi m}{h^2}\right)^{3/2} (k_B T)^{5/2} \xi_{rot}\, \xi_{vib} \times \exp\left[-\frac{\Delta H(0)}{k_B T} - \frac{1}{k_B}\int_0^T \frac{dT'}{T'^2}\int_0^{T'} c_v(T'')dT''\right]$$

where the variables have their usual meaning (m for mass, h for Planck constant, ξ for partition functions, $\Delta H(0)$ for the latent heat of sublimation at absolute zero, and c_v for specific heat capacity at constant volume.) This can be written more succinctly as

$$\ln p = \text{const.} + \frac{f+2}{2}\ln(k_B T) - \frac{\Delta H(0)}{k_B T} - \frac{1}{k_B}\int_0^T \frac{dT'}{T'^2}\int_0^{T'} c_v(T'')dT'' \tag{21}$$

where f is the number of degrees of freedom.

Eq. (21) is straightforward to derive. The energy required to heat a block of ice and then convert it into gas has to be same as when first converted to gas and then heated to the same temperature T:

$$L(T) + \int_0^T c_{\text{solid}}(T')\,dT' = L(0) + \int_0^T c_{\text{gas}}(T')\,dT' \tag{22}$$

It follows,

$$L(T) = L(0) + \int_0^T [c_{\text{gas}}(T') - c_{\text{solid}}(T')]\,dT' \tag{23}$$

The heat capacity of an ideal gas at constant pressure is $c_{\text{gas}} = (1 + f/2)k_B$, where f is the number of degrees of freedom, e.g., $f = 3$ for a monatomic gas, $f = 5$ for a diatomic gas (such as CO) or a linear polyatomic molecule (such as CO_2), and $f = 6$ with a third rotational degree of freedom (such as H_2O). Therefore,

$$L(T) = L(0) + \frac{f+2}{2}k_B T - \int_0^T c_{\text{solid}}(T')\,dT' \tag{24}$$

This provides a physical motivation for the b_2-term in Eq. (3), which leads to the logarithmic term in the temperature dependence of the vapor pressure (4). When Clausius–Clapeyron (1) is applied to Eq. (24), it leads to Eq. (21).

The heat capacity of a solid goes to zero as the absolute temperature goes to zero. At sufficiently low temperature, the heat capacity of the solid is lower than the heat capacity of the gas. According to this argument, b_2 should be positive at very low temperature. For example, for water $f = 6$ and therefore $b_2 = 4$, which implies the vapor pressure has a prefactor of T^4 (Sack and Baragiola, 1993).

References

Appleton, G.T., Van Hook, W.A., 1982. Vapor pressures of some isotopic hydrogen cyanides. J. Chem. Eng. Data 27, 363–365.
Armstrong, G.T., Brickwedde, F.G., Scott, R.B., 1955. Vapor pressures of the methanes. J. Res. Natl. Bur. Stand. 55, 39–52.
Arnold, J.R., 1979. Ice in the lunar polar regions. J. Geophys. Res. 84, 5659–5668. https://doi.org/10.1029/JB084iB10p05659.
Beaumont, R.H., Chihara, H., Morrison, J.A., 1961. Thermodynamic properties of krypton. vibrational and other properties of solid argon and solid krypton. Proc. Phys. Soc. 78, 1462.
Berezhnoy, A.A., Kozlova, E.A., Sinitsyn, M.P., Shangaraev, A.A., Shevchenko, V.V., 2012. Origin and stability of lunar polar volatiles. Adv. Space Res. 50, 1638–1646. https://doi.org/10.1016/j.asr.2012.03.019.
Bielska, K., Havey, D.K., Scace, G.E., Lisak, D., Harvey, A.H., Hodges, J.T., 2013. High-accuracy measurements of the vapor pressure of ice referenced to the triple point. Geophys. Res. Lett. 40, 6303–6307.
Bigeleisen, J., Fuks, S., Ribnikar, S.V., Yato, Y., 1977. Vapor pressures of the isotopic ethylenes. V. solid and liquid ethylene-d 1, ethylene-d 2 (cis, trans, and gem), ethylene-d 3, and ethylene-d 4. J. Chem. Phys. 66, 1689–1700.
Bockelée-Morvan, D., Biver, N., 2017. The composition of cometary ices. Philos. Trans. R. Soc. A 375, 20160252.
Brown, G.N., Ziegler, W.T., 1980. Vapor pressure and heats of vaporization and sublimation of liquids and solids of interest in cryogenics below 1-atm pressure. In: Advances in Cryogenic Engineering. Springer, pp. 662–670.

Bryson, C.E., Cazcarra, V., Levenson, L.L., 1974. Sublimation rates and vapor pressures of H2O, CO2, N2O, and Xe. J. Chem. Eng. Data 19, 107–110. https://doi.org/10.1021/je60061a021.

Burrell, G.A., Robertson, I.W., 1915. The vapor pressures of acetylene, ammonia and isobutane at temperatures below their normal boiling points. J. Am. Chem. Soc. 37, 2482–2486.

Červinka, C., Beran, G.J.O., 2019. Towards reliable ab initio sublimation pressures for organic molecular crystals–are we there yet? Phys. Chem. Chem. Phys. 21, 14799–14810. https://doi.org/10.1039/C9CP01572H.

Clark, A., Crockett, A.H., Eisner, H.S., 1951. The vapour pressure of hydrogen sulphide. Proc. R. Soc. Lond. Ser. A Math. Phys. Eng. Sci. 209, 408–415.

Colaprete, A., Schultz, P., Heldmann, J., Wooden, D., Shirley, M., et al., 2010. Detection of water in the LCROSS ejecta plume. Science 330, 463–468. https://doi.org/10.1126/science.1186986.

Comsa, G., 1968. Angular distribution of scattered and desorbed atoms from specular surfaces. J. Chem. Phys. 48, 3235–3240.

Escribano, R.M., Muñoz Caro, G.M., Cruz-Diaz, G.A., Rodríguez-Lazcano, Y., Maté, B., 2013. Crystallization of CO2 ice and the absence of amorphous CO2 ice in space. Proc. Natl. Acad. Sci. 110, 12899–12904.

Falk, M., 1987. Amorphous solid carbon dioxide. J. Chem. Phys. 86, 560–564.

Feres, R., Yablonsky, G., 2004. Knudsen's cosine law and random billiards. Chem. Eng. Sci. 59, 1541–1556. https://doi.org/10.1016/j.ces.2004.01.016.

Fernández-Fassnacht, E., Del Río, F., 1984. The vapour pressure of CO2 from 194 to 243 K. J. Chem. Thermodyn. 16, 469–474.

Fray, N., Schmitt, B., 2009. Sublimation of ices of astrophysical interest: A bibliographic review. Planet. Space Sci. 57, 2053–2080.

Giauque, W.F., Blue, R.W., 1936. Hydrogen sulfide. the heat capacity and vapor pressure of solid and liquid. the heat of vaporization. a comparison of thermooodynamic and spectroscopic values of the entropy. J. Am. Chem. Soc. 58, 831–837.

Giauque, W.F., Ruehrwein, R.A., 1939. The entropy of hydrogen cyanide. heat capacity, heat of vaporization and vapor pressure. hydrogen bond polymerization of the gas in chains of indefinite length. J. Am. Chem. Soc. 61, 2626–2633.

Giauque, W.F., Stephenson, C.C., 1938. Sulfur dioxide. the heat capacity of solid and liquid. vapor pressure. heat of vaporization. the entropy values from thermal and molecular data. J. Am. Chem. Soc. 60, 1389–1394.

Gibson, Jr., E.K., 1977. Volatile elements, carbon, nitrogen, sulfur, sodium, potassium and rubidium in the lunar regolith. Phys. Chem. Earth 10, 57–62.

Grundy, W.M., Tegler, S.C., Steckloff, J.K., Tan, S.P., Loeffler, M.J., et al., 2023. Laboratory measurement of volatile ice vapor pressures with a quartz crystal microbalance. Icarus 115767. https://doi.org/10.1016/j.icarus.2023.115767.

Hardy, B., 1998. ITS-90 formulations for vapor pressure, frostpoint temperature, dewpoint temperature, and enhancement factors in the range -100 to 100 c. In: Proc. Third Int. Symp. Humidity Moisture. Teddington, London, UK.

Haynes, D.R., Tro, N.J., George, S.M., 1992. Condensation and evaporation of H2O on ice surfaces. J. Phys. Chem. 96, 8502–8509. https://doi.org/10.1021/j100200a055.

Hudson, R.L., Gerakines, P.A., 2023. Infrared spectra and vapor pressures of crystalline C_2N_2, with comparisons to crystalline HCN. Planet. Sci. J. 4, 205. https://doi.org/10.3847/PSJ/ad0040.

Huebner, W.F., Benkhoff, J., Capria, M.T., Coradini, A., Sanctis, C.D., Orosei, R., Prialnik, D., 2006. Heat and gas diffusion in comet nuclei. Int. Space Sci. Inst. (285).

Jenniskens, P., Blake, D.F., Kouchi, A., 1998. Amorphous water ice. In: Schmitt, B., et al. (Eds.), Solar System Ices. Kluwer, pp. 139–155.

Karwat, E., 1924. Der dampfdruck des festen chlorwasserstoffs, methans und ammoniaks. Z. Phys. Chem. 112, 486–490.

Kazakov, A., Muzny, C.D., Kroenlein, K., Diky, V., Chirico, R.D., Magee, J.W., Abdulagatov, I.M., Frenkel, M., 2012. NIST/TRC source data archival system: The next-generation data model for storage of thermophysical properties. Int. J. Thermophys. 33, 22–33.

Knudsen, M., 1909. Die gesetze der molekularströmung und der inneren reibungsströmung der gase durch röhren. Ann. Phys. 333, 75–130.

Landis, M.E., Hayne, P.O., Williams, J.P., Greenhagen, B.T., Paige, D.A., 2022. Spatial distribution and thermal diversity of surface volatile cold traps at the lunar poles. Planet. Sci. J. 3 (39), https://doi.org/10.3847/PSJ/ac4585.

Leger, A., Gauthier, S., Defourneau, D., Rouan, D., 1983. Properties of amorphous H2O ice and origin of the 3.1-micron absorption. Astron. Astrophys. 117, 164–169.

Leming, C.W., Pollack, G.L., 1970. Sublimation pressures of solid Ar, Kr, and Xe. Phys. Rev. B 2, 3323.

Levenson, L.L., 1971. Condensation coefficients of argon, krypton, xenon, and carbon dioxide measured with a quartz crystal microbalance. J. Vacuum Sci. Technol. 8, 629–635.

Liang, S.C., 1952. Low vapor pressure measurement and thermal transpiration. J. Phys. Chem. 56, 660–662.

Linstrom, P.J., Mallard, W.G., 2001. NIST chemistry WebBook: A chemical data resource on the internet. https://doi.org/10.18434/T4D303, URL https://webbook.nist.gov/chemistry/.

Lucas, S., Ferry, D., Demirdjian, B., Suzanne, J., 2005. Vapor pressure and solid phases of methanol below its triple point temperature. J. Phys. Chem. B 109, 18103–18106.

Mandt, K.E., Mousis, O., Hurley, D., Bouquet, A., Retherford, K.D., Magaña, L.O., Luspay-Kuti, A., 2022. Exogenic origin for the volatiles sampled by the lunar crater observation and sensing satellite impact. Nat. Comm. 13, 642. https://doi.org/10.1038/s41467-022-28289-6.

Mauersberger, K., Krankowsky, D., 2003. Vapor pressure above ice at temperatures below 170 K. Geophys. Res. Lett. 30, https://doi.org/10.1029/2002GL016183.

Mullins, J.C., Kirk, B.S., Ziegler, W.T., 1963. Calculation of the vapor pressure and heats of vaporization and sublimation of liquids and solids, especially below one atmosphere pressure. V. In: Carbon Monoxide and Carbon Dioxide. Technical Report, Georgia Institute of Technology, United States.

Mündel, C.F., 1913. Experimentelle bestimmung und theoretische berechnung kleiner dampfdrücke bei tiefen temperaturen. Z. Phys. Chem. 85, 435–465.

Murphy, D.M., Koop, T., 2005. Review of the vapour pressures of ice and supercooled water for atmospheric applications. Q. J. R. Meteorol. Soc. 131, 1539–1565. https://doi.org/10.1256/qj.04.94.

Paige, D.A., Foote, M.C., Greenhagen, B.T., et al., 2010a. The lunar reconnaissance orbiter diviner lunar radiometer experiment. Space Sci. Rev. 150, 125–160. https://doi.org/10.1007/s11214-009-9529-2.

Paige, D.A., Siegler, M.A., Zhang, J.A., et al., 2010b. Diviner lunar radiometer observations of cold traps in the Moon's south polar region. Science 330, 479–482. https://doi.org/10.1126/science.1187726.

Persad, A.H., Ward, C.A., 2016. Expressions for the evaporation and condensation coefficients in the Hertz-Knudsen relation. Chem. Rev. 116, 7727–7767. https://doi.org/10.1021/acs.chemrev.5b00511.

Petro, N.E., Banks, M., Elder, C.M., et al., 2022. The lunar reconnaissance orbiter mission as a new era of lunar exploration begins, plans for extended mission 5. Proc. Lunar Planet. Sci. Conf. 53, 2326.

Reif, F., 1965. Fundamentals of Statistical and Thermal Physics. McGraw-Hill.

Sack, N.J., Baragiola, R.A., 1993. Sublimation of vapor-deposited water ice below 170K, and its dependence on growth conditions. Phys. Rev. B 48, 9973.

Salter, L.S., 1963. Vapour pressure of a monatomic crystal. Trans. Faraday Soc. 59, 657–666.

Schmitt, B., Rodriguez, S., 2003. Possible identification of local deposits of Cl2SO2 on Io from NIMS/Galileo spectra. J. Geophys. Res. Planets 108, https://doi.org/10.1029/2002JE001988.

Schorghofer, N., Williams, J.-P., 2020. Mapping of ice storage processes on the Moon with time-dependent temperatures. Planet. Sci. J. 1 (54), https://doi.org/10.3847/PSJ/abb6ff.

Schorghofer, N., Williams, J.-P., 2024. Replication data for: Sublimation pressures of common volatiles at low temperature maps of supervolatile cold traps on the Moon. https://doi.org/10.7910/DVN/UUIVXQ, Harvard Dataverse.

Schorghofer, N., Williams, J.-P., Martinez-Camacho, J., Paige, D., Siegler, M., 2021. Carbon dioxide cold traps on the Moon. Geophys. Res. Lett. 48, https://doi.org/10.1029/2021GL095533.

Shakeel, H., Wei, H., Pomeroy, J.M., 2018. Measurements of enthalpy of sublimation of Ne, N2, O2, Ar, CO2, Kr, Xe, and H2O using a double paddle oscillator. J. Chem. Thermodyn. 118, 127–138. https://doi.org/10.1016/j.jct.2017.11.004.

Shimizu, H., Nakamichi, Y., Sasaki, S., 1991. Pressure-induced phase transition in solid hydrogen sulfide at 11 GPa. J. Chem. Phys. 95, 2036–2040.

Shimizu, H., Yamaguchi, H., Sasaki, S., Honda, A., Endo, S., Kobayashi, M., 1995. Pressure-temperature phase diagram of solid hydrogen sulfide determined by Raman spectroscopy. Phys. Rev. B 51, 9391–9394.

Souda, R., 2006. Glass-liquid transition of carbon dioxide and its effect on water segregation. J. Phys. Chem. B 110, 17884–17888.

Staveley, L.A.K., Lobo, L.Q., Calado, J.C.G., 1981. Triple-points of low melting substances and their use in cryogenic work. Cryogenics 21, 131–144.

Stern, S.A., 1999. The lunar atmosphere: history, status, current problems, and context. Rev. Geophys. 37, 453–491.

Stull, D.R., 1947a. Vapor pressure of pure substances. inorganic compounds. Ind. Eng. Chem. 39, 540–550.

Stull, D.R., 1947b. Vapor pressure of pure substances. organic compounds. Ind. Eng. Chem. 39, 517–540.

Tegeler, C., Span, R., Wagner, W., 1999. A new equation of state for argon covering the fluid region for temperatures from the melting line to 700 K at pressures up to 1000 MPa. J. Phys. Chem. Ref. Data 28, 779–850.

Tickner, A.W., Lossing, F.P., 1951. The measurement of low vapor pressures by means of a mass spectrometer. J. Phys. Chem. 55, 733–740.

Vogt, G.J., Pitzer, K.S., 1976. Entropy and heat capacity of methane; spin-species conversion. J. Chem. Thermodyn. 8, 1011–1031.

Washburn, E.W., et al. (Eds.), 1933. International Critical Tables of Numerical Data, Physics, Chemistry and Technology. National Research Council, New York and London.

Watson, K., Murray, B.C., Brown, H., 1961. The behavior of volatiles on the lunar surface. J. Geophys. Res. 66, 3033–3045. https://doi.org/10.1029/JZ066i009p03033.

Williams, J.-P., Greenhagen, B.T., Paige, D.A., Schorghofer, N., Sefton-Nash, E., Hayne, P., Lucey, P.G., Siegler, M.A., Aye, K.M., 2019. Seasonal polar temperatures on the Moon. J. Geophys. Res. 124, 2505–2521. https://doi.org/10.1029/2019JE006028.

Williams, J.-P., Sefton-Nash, E., Paige, D.A., 2016. The temperatures of giordano bruno crater observed by the diviner lunar radiometer experiment: Application of an effective field of view model for a point-based data set. Icarus 273, 205–213. https://doi.org/10.1016/j.icarus.2015.10.034.

Yu, X., Yu, Y., Garver, J., Li, J., Hawthorn, A., Sciamma-O'Brien, E., Zhang, X., Barth, E., 2023. Material properties of organic liquids, ices, and hazes on Titan. Astrophys. J. Suppl. Ser. 266, https://doi.org/10.3847/1538-4365/acc6cf.

Zhang, J.A., Paige, D.A., 2009. Cold-trapped organic compounds at the poles of the Moon and Mercury: Implications for origins. Geophys. Res. Lett. 36 (L16203), https://doi.org/10.1029/2009GL038614.

Zhang, J.A., Paige, D.A., 2010. Correction to: cold-trapped organic compounds at the poles of the Moon and Mercury: Implications for origins. Geophys. Res. Lett. 37 (L03203), https://doi.org/10.1029/2009GL041806.

Zheng, W., Kaiser, R.I., 2007. An infrared spectroscopy study of the phase transition in solid ammonia. Chem. Phys. Lett. 440, 229–234. https://doi.org/10.1016/j.cplett.2007.04.070.

Ziegler, W.T., Mullins, J.C., Kirk, B.S., 1962a. Calculation of the Vapor Pressure and Heats of Vaporization and Sublimation of Liquids and Solids, Especially below One Atmosphere Pressure. I. Ethylene. Technical Report, Georgia Institute of Technology, United States.

Ziegler, W.T., Mullins, J.C., Kirk, B.S., 1962b. Calculation of the Vapor Pressure and Heats of Vaporization and Sublimation of Liquids and Solids, Especially below One Atmosphere Pressure. II. Argon. Technical Report, Georgia Institute of Technology, United States.

Ziegler, W.T., Mullins, J.C., Kirk, B.S., 1962c. Calculation of the Vapor Pressure and Heats of Vaporization and Sublimation of Liquids and Solids, Especially below One Atmosphere Pressure. III. Methane. Technical Report, Georgia Institute of Technology, United States.